

Spin-valley-coupled quantum spin Hall insulator with topological Rashba-splitting edge states in Janus monolayer $\text{CSb}_{1.5}\text{Bi}_{1.5}$

San-Dong Guo

School of Electronic Engineering, Xi'an University of Posts and Telecommunications, Xi'an 710121, China

Achieving combination of spin and valley polarized states with topological insulating phase is pregnant to promote the fantastic integration of topological physics, spintronics and valleytronics. In this work, a spin-valley-coupled quantum spin Hall insulator (svc-QSHI) is predicted in Janus monolayer $\text{CSb}_{1.5}\text{Bi}_{1.5}$ with dynamic, mechanical and thermal stabilities. The inequivalent valleys have opposite Berry curvature and spin moment, which can produce a spin-valley Hall effect. In the center of Brillouin zone, a Rashba-type spin splitting can be observed due to missing horizontal mirror symmetry. Moreover, monolayer $\text{CSb}_{1.5}\text{Bi}_{1.5}$ shows unique Rashba-splitting edge states. Both energy band gap and spin-splitting at the valley point are larger than the thermal energy of room temperature (25 meV) with generalized gradient approximation (GGA) level, which is very important at room temperature for device applications. It is proved that the spin-valley-coupling and nontrivial quantum spin Hall (QSH) state are robust again biaxial strain. Our work may provide a new platform to achieve integration of topological physics, spintronics and valleytronics.

Keywords: Valley, Spin, Topological insulator, Janus structure

Email:sandongyuwang@163.com

I. INTRODUCTION

Since the valley-dependent effects are discovered in MoS_2 monolayer with missing inversion symmetry, the field of valleytronics is truly flourishing¹⁻³. For hexagonal two-dimensional (2D) materials like monolayer MoS_2 , the conically shaped valleys at $-K$ and K corners are inequivalent, and the spin polarizations are opposite, as the two points are connected by the time reversal symmetry operation. The combination of inversion symmetry breaking and spin-orbit coupling (SOC) can remove spin degeneracy, and then gives rise to valley-contrasting spin splitting, which is the foundation for spin-valleytronics. With an applied in-plane electric field, the charge carriers with opposite valley and spin indexes will attain opposite anomalous transverse velocity, and then a simultaneous spin and valley Hall effect is produced⁴⁻⁶.

On the other hand, the topological insulator (TI) has spin-momentum-locked conducting edge states and insulating properties in the bulk, whose charge and spin transport in the edge states are quantized dissipationless^{7,8}. These bring possibilities for low-dissipation electronic devices. For 2D materials, the TI is also called as QSH insulator (QSHI) characterized by counter-propagating edge currents with opposite spin polarization, which is firstly predicted in graphene⁹. Experimentally confirmed QSHIs include the HgTe/CdTe and InAs/GaSb quantum wells^{10,11}, and many other 2D materials have been proposed as QSHIs by the first-principles calculations¹²⁻¹⁷. To this end, it's a natural idea to achieve the integration of QSHI with spin-valleytronics (namely, svc-QSHI).

Several AB_3 type atomic sheets have been experimentally synthesized, for example BC_3 nanosheets¹⁸. Recently, 2D AB_3 monolayers have also been theoretically reported¹⁹⁻²². The CP_3 monolayer can be used as anode for sodium-ion batteries¹⁹, and the massless Dirac-Fermions can be achieved in CAs_3 monolayer²⁰. In addition to this, the QSHIs and topological Rashba-splitting edge states in monolayer CX_3 ($\text{X}=\text{Sb}$ and Bi) with inversion symmetry have been predicted²². The MoS_2 with 1T' phase is a QSHI, and the corresponding Janus structures MoSSe can still possess nontrivial topology tuned by strain²³. Compared to MoS_2 , the MoSSe will lose inversion symmetry. Inspiring from this, we construct Janus monolayer $\text{CSb}_{1.5}\text{Bi}_{1.5}$ based on monolayer CX_3 ($\text{X}=\text{Sb}$ and Bi). By first principles simulations, we show that Janus monolayer $\text{CSb}_{1.5}\text{Bi}_{1.5}$ is a svc-QSHI with topological Rashba-splitting edge states. Calculated results show these novel features are robust again biaxial strain. These results make monolayer $\text{CSb}_{1.5}\text{Bi}_{1.5}$ an appealing original quantum material for topological physics, spintronics and valleytronics.

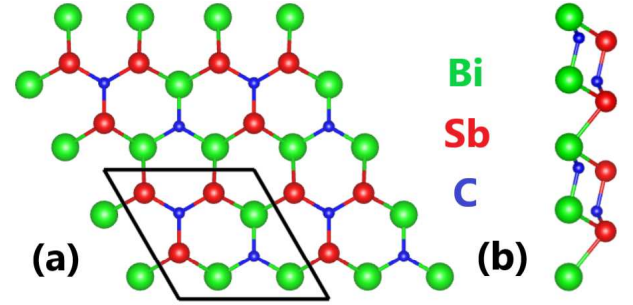


FIG. 1. (Color online) The crystal structure of Janus monolayer $\text{CSb}_{1.5}\text{Bi}_{1.5}$: top view (a) and side view (b). The rhombus primitive cell is shown by black frames in (a).

tion to this, the QSHIs and topological Rashba-splitting edge states in monolayer CX_3 ($\text{X}=\text{Sb}$ and Bi) with inversion symmetry have been predicted²². The MoS_2 with 1T' phase is a QSHI, and the corresponding Janus structures MoSSe can still possess nontrivial topology tuned by strain²³. Compared to MoS_2 , the MoSSe will lose inversion symmetry. Inspiring from this, we construct Janus monolayer $\text{CSb}_{1.5}\text{Bi}_{1.5}$ based on monolayer CX_3 ($\text{X}=\text{Sb}$ and Bi). By first principles simulations, we show that Janus monolayer $\text{CSb}_{1.5}\text{Bi}_{1.5}$ is a svc-QSHI with topological Rashba-splitting edge states. Calculated results show these novel features are robust again biaxial strain. These results make monolayer $\text{CSb}_{1.5}\text{Bi}_{1.5}$ an appealing original quantum material for topological physics, spintronics and valleytronics.

II. COMPUTATIONAL DETAIL

Within density functional theory (DFT)²⁴, we perform the first-principles calculations using the projected augmented wave (PAW) method, as implemented in the

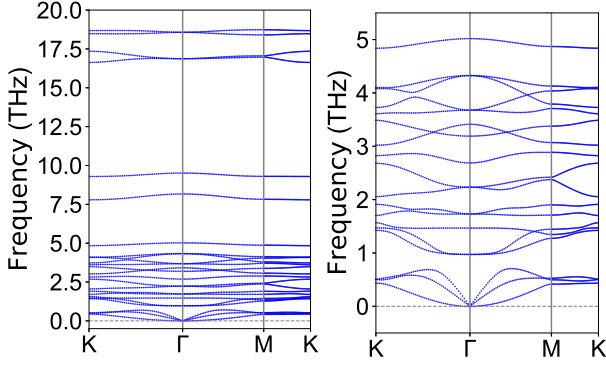


FIG. 2. (Color online) The phonon dispersions (Left) of Janus monolayer $\text{CSb}_{1.5}\text{Bi}_{1.5}$ using GGA with the enlarged views of low frequency (Right).

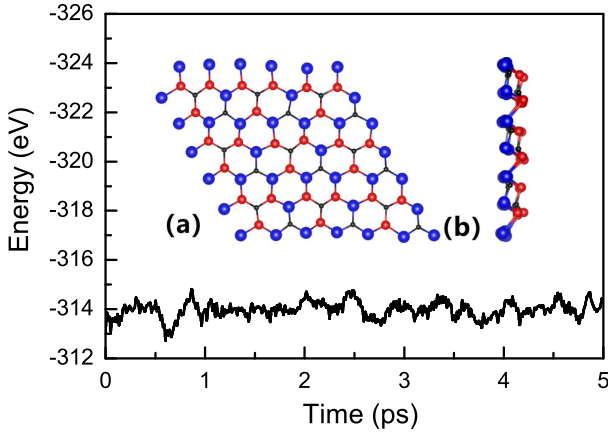


FIG. 3. (Color online) The variation of free energy during the 5 ps AIMD simulation of Janus monolayer $\text{CSb}_{1.5}\text{Bi}_{1.5}$. Insets show the final structures (top view (a) and side view (b)) of $\text{CSb}_{1.5}\text{Bi}_{1.5}$ after 5 ps at 300 K.

VASP package^{25–27}. We use GGA of Perdew, Burke and Ernzerhof (GGA-PBE)²⁸ as the exchange-correlation potential. The cutoff energy for plane-wave expansion is 500 eV with the total energy convergence criterion being 10^{-7} eV. To avoid interactions between two neighboring images, the vacuum region along the z direction is set to be larger than 18 Å. The SOC is incorporated for

TABLE I. For Janus monolayer $\text{CSb}_{1.5}\text{Bi}_{1.5}$, the lattice constants a_0 (Å); the structural parameters including: C-Sb (d_1) and C-Bi (d_2) bond lengths (Å), Sb-C-Sb (θ_1) and Bi-C-Bi (θ_2) bond angles ($^\circ$), the thickness layer height (t) (Å); the elastic constants C_{ij} (Nm^{-1}); shear modulus G_{2D} (Nm^{-1}); Young's modulus C_{2D} (Nm^{-1}); Poisson's ratio ν_{2D} .

a_0	d_1	d_2	θ_1	θ_2	t
7.772	2.131	2.217	115.442	115.154	1.901
C_{11}/C_{22}	C_{12}	G_{2D}	C_{2D}	ν_{2D}	
26.01	9.13	8.44	22.81	0.351	

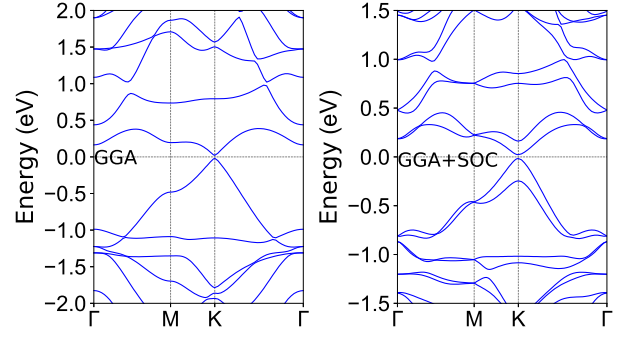


FIG. 4. (Color online) The energy band structures of Janus monolayer $\text{CSb}_{1.5}\text{Bi}_{1.5}$ using GGA and GGA+SOC.

band structure calculations. The Brillouin zone is sampled by using a $12 \times 12 \times 1$ K-point meshes for geometry optimization, elastic coefficients and self-consistent electronic structure calculations. The geometry optimization is considered to be converged, when the residual force on each atom is less than $0.0001 \text{ eV} \cdot \text{Å}^{-1}$. Phonon dispersion spectrum is attained by the Phonopy code²⁹ based on finite displacement method using a $5 \times 5 \times 1$ supercell. The Z_2 invariants are used to investigate topological properties of Janus monolayer $\text{CSb}_{1.5}\text{Bi}_{1.5}$, as implemented by the Wannier90 and WannierTools codes^{30,31}, where a tight-binding Hamiltonian with the maximally localized Wannier functions is fitted to the first-principles band structures. We use PYPROCAR code to obtain the constant energy contour plots of the spin texture³².

III. CRYSTAL AND ELECTRONIC STRUCTURES

Based on DFT calculations, the optimized lattice parameters of Janus monolayer $\text{CSb}_{1.5}\text{Bi}_{1.5}$ is 7.772 Å, which is between ones of CSb_3 (7.58 Å) and CBi_3 (7.96 Å)²². As shown in Figure 1 with top and side views, each C atom forms three C-Sb or C-Bi bonds with three neighboring Sb or Bi atoms, and each Sb/Bi atom forms two Sb-Bi bonds and one C-Sb/Bi bond with neighboring Bi/Sb and C atoms, respectively. The symmetry of Janus monolayer $\text{CSb}_{1.5}\text{Bi}_{1.5}$ with space group $P3m1$ (No.156) is lower than that of $\text{CSb}_3/\text{CBi}_3$ monolayer with space group $P3m1$ (No.164) due to the lack of space inversion symmetry. Monolayer $\text{CSb}_3/\text{CBi}_3$ is composed of two C atomic layers sandwiched between Sb/Bi atomic layers. Similar to Janus monolayer MoSSe from MoS_2 ^{33,34}, the Janus monolayer $\text{CSb}_{1.5}\text{Bi}_{1.5}$ can be constructed by replacing one of two Sb/Bi layers with Bi/Sb atoms in monolayer $\text{CSb}_3/\text{CBi}_3$. For Janus monolayer $\text{CSb}_{1.5}\text{Bi}_{1.5}$, the inequivalent C-Sb and C-Bi bond lengths (Sb-C-Sb and Bi-C-Bi bond angles) will be induced due to the difference in atomic sizes and electronegativities of Sb and Bi atoms, and they are 2.131 Å and 2.217 Å (115.442° and 115.154°), which gives rise

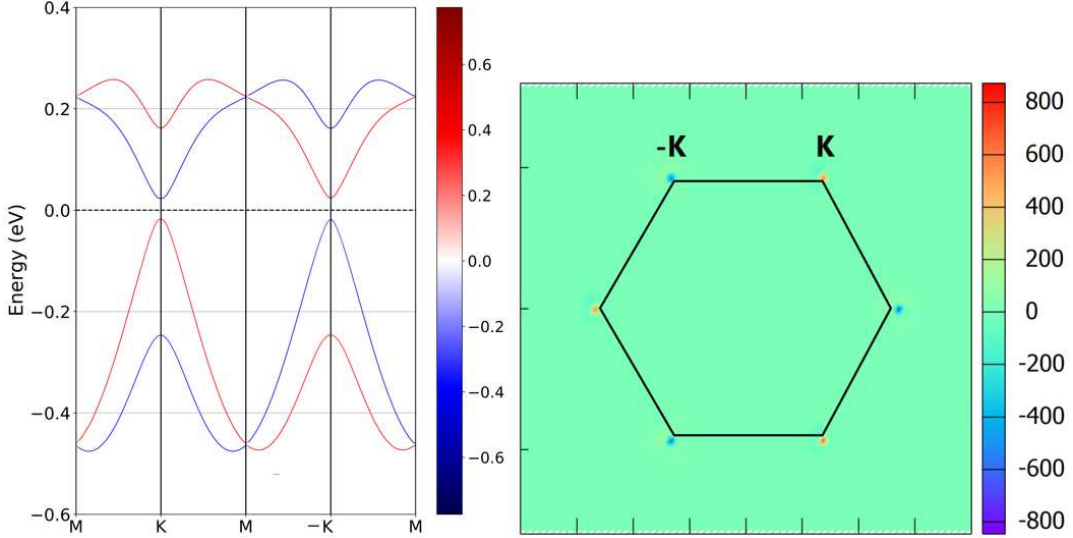


FIG. 5. (Color online) (Left) The color map of the band structure of Janus monolayer $\text{CSb}_{1.5}\text{Bi}_{1.5}$ with the projection of spin operator \hat{S}_z , and the red and blue colors indicate the spin-up and spin-down bands, respectively. (Right) Calculated Berry curvature distribution of Janus monolayer $\text{CSb}_{1.5}\text{Bi}_{1.5}$ in the 2D Brillouin zone.

to a built-in electric field. The symmetry reduce will induce Rashba spin splitting, valley degree of freedom and piezoelectric polarizations.

To confirm the stability of Janus monolayer $\text{CSb}_{1.5}\text{Bi}_{1.5}$, phonon spectra, ab initio molecular dynamics (AIMD) simulations and elastic constants C_{ij} are carried out. Figure 2 shows that all phonon branches have no imaginary frequency in the entire Brillouin zone, suggesting its dynamical stability. It is noted that two in-plane acoustic branches show linear dispersions, while the ZA branch corresponding to the out-of-plane vibrations displays a quadratic dispersion. These conform to quadratic dispersion of ZA phonon branch, when a 2D material is free of stress^{35,36}. The optical branches are well separated from acoustic branches with a gap of 0.29 THz, which prohibits the scattering between acoustic and optical phonon modes. The vibration of the O atoms are mainly at high frequency region. As shown in Figure 3, after heating at 300 K for 5 ps, neither structure reconstruction nor bond breaking with small energy fluctuations for monolayer $\text{CSb}_{1.5}\text{Bi}_{1.5}$ is observed, suggesting its thermal stability.

Using Voigt notation, the 2D elastic tensor with space group $P3m1$ can be reduced into:

$$C = \begin{pmatrix} C_{11} & C_{12} & 0 \\ C_{12} & C_{11} & 0 \\ 0 & 0 & (C_{11} - C_{12})/2 \end{pmatrix} \quad (1)$$

The two independent elastic constants of monolayer $\text{CSb}_{1.5}\text{Bi}_{1.5}$ are $C_{11}=26.01 \text{ Nm}^{-1}$ and $C_{12}=9.13 \text{ Nm}^{-1}$. The shear modulus G^{2D} equals to C_{66} , which can be attained by $(C_{11}-C_{12})/2$, and the corresponding value is 8.44 Nm^{-1} . The calculated C_{ij} satisfy the Born criteria of mechanical stability of a material with hexagonal

symmetry³⁷: $C_{11} > 0$ and $C_{66} > 0$, confirming its mechanical stability. The Young's modulus $C_{2D}(\theta)$ can be calculated by the following equation³⁸:

$$C_{2D}(\theta) = \frac{C_{11}C_{22} - C_{12}^2}{C_{11}\sin^4\theta + A\sin^2\theta\cos^2\theta + C_{22}\cos^4\theta} \quad (2)$$

where $A = (C_{11}C_{22} - C_{12}^2)/C_{66} - 2C_{12}$. The monolayer $\text{CSb}_{1.5}\text{Bi}_{1.5}$ is mechanically isotropic due to hexagonal symmetry, and the C_{2D} is 22.81 Nm^{-1} , which is obviously smaller than those of other 2D materials³⁹⁻⁴¹, suggesting that monolayer $\text{CSb}_{1.5}\text{Bi}_{1.5}$ is more flexible than other 2D materials. The Poisson's ratio $\nu_{2D}(\theta)$ is also isotropic, and can be simply written as:

$$\nu_{2D} = \frac{C_{12}}{C_{11}} \quad (3)$$

The calculated ν_{2D} of monolayer $\text{CSb}_{1.5}\text{Bi}_{1.5}$ is 0.351. The related data are summarized in Table I.

Next, we provide some suggestions on experimental aspects. Firstly, the $\text{CSb}_3/\text{CBi}_3$ monolayer may be experimentally achieved by the bottom-up approaches such as the molecular beam epitaxy (MBE)²², because the epitaxial BC_3 sheet with a similar structure has been successfully synthesized¹⁸. Similar to Janus monolayer MoSSe from MoS_2 ^{33,34}, the Janus monolayer $\text{CSb}_{1.5}\text{Bi}_{1.5}$ can be synthesized experimentally with similar experimental techniques based on $\text{CSb}_3/\text{CBi}_3$ monolayer.

IV. ELECTRONIC STRUCTURES

The energy band structures of Janus monolayer $\text{CSb}_{1.5}\text{Bi}_{1.5}$ with both GGA and GGA+SOC are plotted in Figure 4. In the absence of SOC, one observes

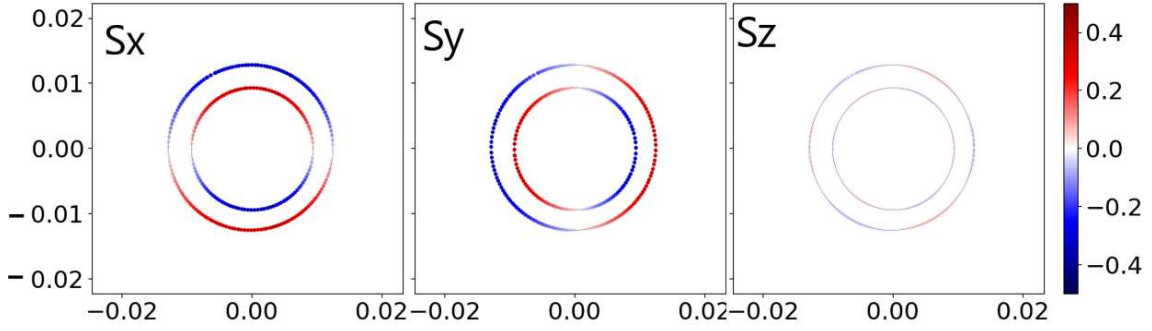


FIG. 6. (Color online) Spin texture of Janus monolayer $\text{CSb}_{1.5}\text{Bi}_{1.5}$ calculated in the 2D Brillouin zone centered at the Γ point and at an energy surface of 0.25 eV above the Fermi level. The red and blue colours show spin-up and spin-down states, respectively.

that $\text{CSb}_{1.5}\text{Bi}_{1.5}$ is a direct band-gap semiconductor with both conduction-band minimum (CBM) and valence-band maximum (VBM) at K point with a gap of 39.9 meV. This is different from that of $\text{CSb}_3/\text{CBi}_3$ with gapless Dirac points at K points due to symmetry reduce. Based on the projected band states to atomic orbitals, the states near the band edges are dominated by the $C-p_z$ orbitals and the $\text{Sb/Bi-}p$ orbitals. When considering SOC, one observes that $\text{CSb}_{1.5}\text{Bi}_{1.5}$ is still a direct band-gap semiconductor with a gap of 40.1 meV. The main SOC effect is to give rise to a spin splitting of the GGA bands. From the symmetry perspective, the inversion symmetry breaking lifts the spin degeneracy at each generic k point. For $\text{CSb}_3/\text{CBi}_3$, no spin degeneracy is removed within SOC due to existing inversion symmetry²². The spin-splitting at the K point is as large as 139 meV (ΔC) and 229 meV (ΔV) for the lowermost conduction band (LCB) and uppermost valence band (UVB), respectively. These splitting energies are very greater than the thermal energy of room temperature (25 meV), which is highly desirable for avoiding spin-flip scattering in spintronics applications.

It should be noted that the conically shaped conduction (valence) band valleys of Janus monolayer $\text{CSb}_{1.5}\text{Bi}_{1.5}$ at K and -K corners are inequivalent but related by time-reversal symmetry. We redraw the energy band structures with the projection of spin operator \hat{S}_z , including -K high symmetry point (See Figure 5). It is clearly seen that the spin polarizations at K and -K are opposite, which means that the low-energy states in the K and -K valleys can be distinguished by their spin index. Once the K and -K valleys are separated with a valley polarization, 100% out-of-plane spin polarization can be realized in transport. The missing inversion symmetry will make these valleys acquire a valley-contrasting Berry curvature $\Omega_z(k)$:

$$\Omega_z(k) = \nabla_k \times i \langle \mu_{n,k} | \nabla_k \mu_{n,k} \rangle \quad (4)$$

in which $\mu_{n,k}$ is the lattice periodic part of the Bloch wave functions. The distribution of Berry curvature in the momentum space for monolayer $\text{CSb}_{1.5}\text{Bi}_{1.5}$ is plotted in Figure 5. It is clearly seen that two obvious peaks

at both K and -K valleys but with opposite sign appear, and the distribution of $\Omega_z(k)$ exhibits a three-fold rotational symmetry. It is not possible to distinguish these two kinds of valleys from energy, but can discern them by their opposite Berry curvatures and out-of-plane spin moments. This will lead to spin-valley-coupled transport properties. When the in-plane electric field is applied, the valley Hall and spin Hall effects would occur simultaneously due to the valley index being coupled with spin (The charge carriers of different valleys flow to the opposite transverse edges due to $v \sim E \times \Omega_z(k)$), resulting in both valley and spin polarization along the edges, namely spin-valley Hall effect.

Moreover, due to the lack of the horizontal mirror symmetry, Janus monolayer $\text{CSb}_{1.5}\text{Bi}_{1.5}$ should have Rashba effect. To examine the Rashba effect, the in-plane spin-textures are calculated, and the Figure 6 shows the spin projected constant energy (0.25 eV above the Fermi level) contour plots of the spin textures calculated in k_x - k_y plane centered at the Γ point. It is clearly seen that the pair of spin-splitting bands for both S_x and S_y spin components have opposite spin orientation. The pure 2D Rashba spin splitting at the conduction bands around Γ point near the Fermi level is observed due to existing concentric spin-texture circles. It is found that only in-plane S_x and S_y spin components are present in the Rashba spin split bands with missing out-of-plane S_z component. The in-plane spin moments of two rings have opposite chirality. The large ring is clockwise, while the small ring is anticlockwise.

The monolayer $\text{CSb}_3/\text{CBi}_3$ is predicted to be a QSHI²². It is natural to confirm the topological properties of Janus monolayer $\text{CSb}_{1.5}\text{Bi}_{1.5}$, which can be characterized by the Z_2 topological invariant. For a material with space inversion symmetry, the Z_2 can be calculated by calculating the parities of the occupied valence bands by using Fu and Kane's method⁴², like monolayer $\text{CSb}_3/\text{CBi}_3$ ²². The universal method is to calculate the Wannier Charge Centers (WCCs), which is used for monolayer $\text{CSb}_{1.5}\text{Bi}_{1.5}$. The evolution of WCCs for monolayer $\text{CSb}_{1.5}\text{Bi}_{1.5}$ is plotted in Figure 7. Taking an arbitrary horizontal line (e.g. $\text{WCC}=0.13$) as ref-

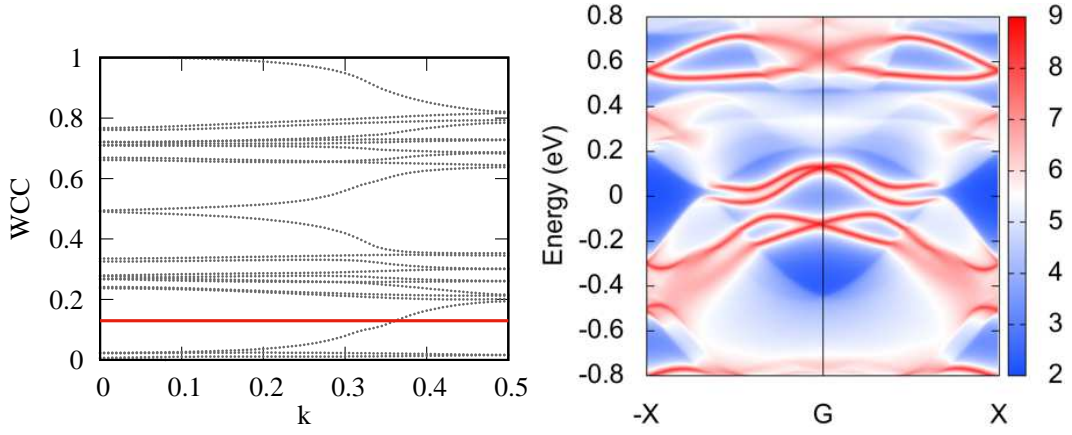


FIG. 7. (Color online) (Left) Evolution of the WCCs and (Right) topological edge states connecting the conduction and valence bands of Janus monolayer $\text{CSb}_{1.5}\text{Bi}_{1.5}$.

erence, one can see that the number of crossings between the reference line and the evolution of WCCs is odd, which verifies that $Z_2=1$. This means that Janus monolayer $\text{CSb}_{1.5}\text{Bi}_{1.5}$ is a QSHI. Furthermore, a QSHI should exhibit topological protected conducting helical edge states. The Green's-function method is used to calculate the edge states on (100) edge based on the tight-binding Hamiltonian, which are shown in Figure 7. It is clearly seen that there is a pair of gapless non-trivial edge states, which connect the conduction and valence bands. The edge states exhibit two quadratic dispersive branches with opposite spin. The Dirac point is pushed above the Fermi level, and the Rashba-like splitting states can be observed. Similar phenomenon can be found in monolayer CSb_3 ²².

In practical application, a substrate is likely to introduce strain to a 2D material due to lattice mismatch. A biaxial in-plane strain is used to study the robustness of the related physical properties of Janus monolayer $\text{CSb}_{1.5}\text{Bi}_{1.5}$ against the strain effects. We use a/a_0 (0.94-1.06) to simulate biaxial in-plane strain, where a and a_0 represent the in-plane lattice constants with and without strain, respectively. The strained energy band structures with both GGA and GGA+SOC are plotted in FIG.1 and FIG.2 of electronic supplementary information (ESI). Except for 0.94 strain, they all show direct band-gap semiconductors with both CBM and VBM at K point. For 0.94 strain, GGA results show a metal, but GGA+SOC results demonstrate an indirect band-gap semiconductor with CBM and VBM at Γ and K points. The energy band gaps with both GGA and GGA+SOC and spin-splittings at the K point for LCB and UVB as a function of strain are plotted in FIG.3 and FIG.4 of ESI. These gaps (except for 0.94 strain) and spin-splittings are greater than the thermal energy of room temperature (25 meV), which is necessary to readily access and

manipulate valleys for memory and logic applications. Finally, we calculate Z_2 at all strain points to confirm topological properties of strained monolayer $\text{CSb}_{1.5}\text{Bi}_{1.5}$, and only show the evolution of WCCs at 0.94 and 1.06 strains in FIG.5 of ESI. The calculated results show that the WCCs can be crossed only one time by an arbitrary horizontal line, which means $Z_2=1$. These confirm that all strained monolayer $\text{CSb}_{1.5}\text{Bi}_{1.5}$ are TIs. These imply that the spin-valley coupling and nontrivial topological state are robust against the biaxial strain.

V. DISCUSSIONS AND CONCLUSION

In summary, our calculated results demonstrate that svc-QSHI with spin and valley polarized states can emerge in the Janus monolayer $\text{CSb}_{1.5}\text{Bi}_{1.5}$. Particularly, the $\text{CSb}_{1.5}\text{Bi}_{1.5}$ monolayer hosts Rashba-splitting edge states, which can be measured by angle-resolved photoemission spectroscopy (ARPES). Furthermore, we demonstrate that the spin-valley-coupling and topological properties are perfectly preserved, when a suitable biaxial strain is applied. In view of the recent experimental progress in AB_3 type atomic sheets¹⁸ and Janus monolayers^{33,34}, our findings can promote further experimental exploration for intriguing svc-QSHI.

ACKNOWLEDGMENTS

This work is supported by Natural Science Basis Research Plan in Shaanxi Province of China (2021JM-456). We are grateful to the Advanced Analysis and Computation Center of China University of Mining and Technology (CUMT) for the award of CPU hours and WIEN2k/VASP software to accomplish this work.

¹ D. Xiao, G. B. Liu, W. Feng, X. Xu and W. Yao, Phys. Rev. Lett. **108**, 196802 (2012).

² K. F. Mak, K. L. McGill, J. Park and P. L. McEuen, Science **344**, 1489 (2014).

- ³ J. R. Schaibley, H. Yu, G. Clark, P. Rivera, J. S. Ross, K. L. Seyler, W. Yao and X. Xu, *Nat. Rev. Mater.* **1**, 16055 (2016).
- ⁴ D. Xiao, W. Yao and Q. Niu, *Phys. Rev. Lett.* **99**, 236809 (2007).
- ⁵ M. Ezawa, *Phys. Rev. B* **87**, 155415 (2013).
- ⁶ Z. F. Liu, W. X. Feng, H. L. Xin, Y. L. Gao, P. F. Liu, Y. G. Yao, H. M. Weng and J. J. Zhao, *Mater. Horiz.* **6**, 781 (2019).
- ⁷ M. Z. Hasan and C. L. Kane, *Rev. Mod. Phys.* **82**, 3045 (2010).
- ⁸ X. L. Qi and S. C. Zhang, *Rev. Mod. Phys.* **83**, 1057 (2011).
- ⁹ C. L. Kane and E. J. Mele, *Phys. Rev. Lett.* **95**, 226801 (2005).
- ¹⁰ M. König, S. Wiedmann, C. Brune et al., *Science* **318**, 766 (2007).
- ¹¹ I. Knez, R. R. Du and G. Sullivan, *Phys. Rev. Lett.* **107**, 136603 (2011).
- ¹² C. C. Liu, W. Feng and Y. Yao, *Phys. Rev. Lett.* **107**, 076802 (2011).
- ¹³ S. Zhou, C. C. Liu, J. J. Zhao and Y. G. Yao, *npj Quant. Mater.* **3**, 16 (2018).
- ¹⁴ S. Murakami, *Phys. Rev. Lett.* **97**, 236805 (2006).
- ¹⁵ J. J. Zhou, W. X. Feng, C. C. Liu, S. Guan and Y. G. Yao, *Nano Lett.* **14**, 4767 (2014).
- ¹⁶ Y. Xu, B. Yan, H. J. Zhang et al., *Phys. Rev. Lett.* **111**, 136804 (2013).
- ¹⁷ H. M. Weng, X. Dai and Z. Fang, *Phys. Rev. X* **4**, 011002 (2014).
- ¹⁸ H. Yanagisawa, Y. Ishida, T. Tanaka, A. Ueno, S. Otani and C. Oshima, *Surf. Sci.* **600**, 4072 (2006).
- ¹⁹ Z. Zhao, T. Yu, S. Zhang, H. Xu, G. Yang and Y. Liu, *J. Mater. Chem. A* **7**, 405 (2019).
- ²⁰ C. Kamal, *Phys. Rev. B* **100**, 205404 (2019).
- ²¹ M. S. Ramzan, V. Bacic, Y. Jing and A. Kuc, *J. Phys. Chem. C* **123**, 25470 (2019).
- ²² S. S. Wang, W. C. Sun and S. Dong, *Phys. Chem. Chem. Phys.* **23**, 2134 (2021).
- ²³ H. W. Xu, H. Wang, J. Zhou, Y. F. Guo, J. Kong and J. Li, *npj Computational Materials* **7**, 31 (2021).
- ²⁴ P. Hohenberg and W. Kohn, *Phys. Rev.* **136**, B864 (1964); W. Kohn and L. J. Sham, *Phys. Rev.* **140**, A1133 (1965).
- ²⁵ G. Kresse, *J. Non-Cryst. Solids* **193**, 222 (1995).
- ²⁶ G. Kresse and J. Furthmüller, *Comput. Mater. Sci.* **6**, **15** (1996).
- ²⁷ G. Kresse and D. Joubert, *Phys. Rev. B* **59**, 1758 (1999).
- ²⁸ J. P. Perdew, K. Burke and M. Ernzerhof, *Phys. Rev. Lett.* **77**, 3865 (1996).
- ²⁹ A. Togo, F. Oba, and I. Tanaka, *Phys. Rev. B* **78**, 134106 (2008).
- ³⁰ Q. Wu, S. Zhang, H. F. Song, M. Troyer and A. A. Soluyanov, *Comput. Phys. Commun.* **224**, 405 (2018).
- ³¹ A. A. Mostofia, J. R. Yatesb, G. Pizzif, Y.-S. Lee, I. Souzad, D. Vanderbilt and N. Marzarif, *Comput. Phys. Commun.* **185**, 2309 (2014).
- ³² U. Herath, P. Tavadze, X. He, E. Bousquet, S. Singh, F. Munoz and A. H. Romero, *Computer Physics Communications* **251**, 107080 (2020).
- ³³ A.-Y. Lu, H. Zhu, J. Xiao, C.-P. Chuu, Y. Han, M.-H. Chiu, C.-C. Cheng, C.-W. Yang, K.-H. Wei, Y. Yang, Y. Wang, D. Sokaras, D. Nordlund, P. Yang, D. A. Muller, M.-Y. Chou, X. Zhang and L.-J. Li, *Nat. Nanotechnol.* **12**, 744 (2017).
- ³⁴ J. Zhang, S. Jia, I. Kholmanov, L. Dong, D. Er, W. Chen, H. Guo, Z. Jin, V. B. Shenoy, L. Shi and J. Lou, *ACS Nano* **11**, 8192 (2017).
- ³⁵ E. Mariani and F. V. Oppen, *Phys. Rev. Lett.* **100**, 076801 (2008).
- ³⁶ J. Carrete, W. Li, L. Lindsay, D. A. Broido, L. J. Gallego and N. Mingo, *Mater. Res. Lett.* **4**, 204 (2016).
- ³⁷ R. C. Andrew, R. E. Mapasha, A. M. Ukpong and N. Chetty, *Phys. Rev. B* **85**, 125428 (2012).
- ³⁸ E. Cadelano, P. L. Palla, S. Giordano and L. Colombo, *Phys. Rev. B* **82**, 235414 (2010).
- ³⁹ L. Dong, J. Lou and V. B. Shenoy, *ACS Nano*, **11**, 8242 (2017).
- ⁴⁰ M. N. Blonsky, H. L. Zhuang, A. K. Singh and R. G. Hennig, *ACS Nano*, **9**, 9885 (2015).
- ⁴¹ S. D. Guo, Y. T. Zhu, W. Q. Mu and W. C. Ren, *EPL* **132**, 57002 (2020).
- ⁴² L. Fu and C. L. Kane, *Phys. Rev. B* **76**, 045302 (2007).